International Forum on Aeroelasticity and Structural Dynamics
IFASD 2024
17-21 June 2024, The Hague, The Netherlands

# WIND TUNNEL TESTING ACTIVE GUST LOAD ALLEVIATION OF A FLEXIBLE WING

**Felix Stalla*[1], Thiemo M. Kier[1], Gertjan Looye[1], Kolja Michel[1], Thomas G. Schmidt[2], Charlotte Hanke[2], Johannes Dillinger[2], Markus Ritter[2], Martin Tang[2]**

[1]German Aerospace Center (DLR), Institute of System Dynamics and Control
Münchener Str. 20, 82234, Wessling, Germany
* felix.stalla@dlr.de

[2]German Aerospace Center (DLR), Institute of Aeroelasticity
Bunsenstraße 10, 37073 Göttingen, Germany

**Keywords:** gust load alleviation, aeroservoelasticity, wind tunnel testing, robust control

**Abstract:** Increasing efficiency is at the core of next generation aircraft development. Aerodynamics can be improved by high aspect ratio wings, but as these wings are more susceptible to loads from gusts and maneuvers, structural weight might increase. Active load control enables the use of high aspect ratio wings while maintaining a relatively low structural weight. To enhance the technology readiness of such secondary flight control functions, experiments are indispensable. This paper describes the wind tunnel testing of a gust load alleviation controller on a flexible swept wing, equipped with multiple trailing edge flaps and acceleration sensors. Disturbances are injected by a gust generator located upstream of the model. The complete process leading up to the active control experiment is outlined: the simulation model used for controller development, the experimental identification of the system and updating of said model, the controller design, and the validation in the wind tunnel. $\mu$-synthesis robust control is used, achieving the best possible performance with respect to the uncertainties in the system. The robust controller achieves a significant load reduction of up to 80% in the wind tunnel tests.

## 1 INTRODUCTION

In-flight loads are a key driver of a transport aircraft's structural weight. High loads arise during maneuvers, gusts or turbulence. Active control technologies are a promising approach for load alleviation in these cases. Such technologies are of particular interest when applied on high aspect ratio wings. If it is possible to reduce the maximum loads occurring in flight, aircraft can be built lighter, positively affecting fuel efficiency, emissions, and environmental impact. Measures to apply maneuver load alleviation (MLA) and gust load alleviation (GLA) in combination yield synergy effects, improving the possible weight reduction, targeting the sizing loads for each section of the wing [1, 2].

Load alleviation functions are already implemented in a number of large civil and military aircraft, for example the Northrop B-2, the Lockheed C-5, the Lockheed L-1011, the Boeing 787 and all Airbus aircraft since the development of the A320 [3]. Most of these functions rely on inertial sensors placed in the fuselage of the aircraft, comparing commanded and measured acceleration, thus being an addition to the existing primary flight control system. [3, 4]. Current research is conducted on separating the rigid body motion of the entire aircraft from the flexible motion of the wings due to the gust or maneuver encounter, using sensors placed on the wing.

This allows to address the loads occurring at the wing root more effectively. Additionally, with advancements in automatic control and novel control methods, the performance and robustness of load alleviation functionalities can be increased. Several control methods have been applied to load alleviation problems lately, like robust control [5], incremental nonlinear dynamic inversion [6], or $H_2$-optimal blending [7]. Further research is devoted to gust anticipation, for example using a LIDAR sensor [8]. Such feedfoward information can be used in addition to the feedback control functionalities, improving performance. Then, model predictive control [9] presents another suitable control methodology.

A key challenge in the development of load alleviation functions is to ensure not only performance, but also the applicability under realistic operating conditions. The most important factors to take into account are uncertainties in air flow (uncertain atmospheric conditions), degrading sensor and actuator precision, and an overall mismatch of the aircraft's model used in controller design and the actual aircraft. To investigate the practical applicability of gust load controllers, experiments are indispensable. Wind tunnel as well as flight tests are an important part in current research activities [10, 11].

This paper describes the design and wind tunnel testing of a GLA controller. The paper outlines all the steps conducted to validate the developed controller experimentally, ensuring the controller can cope with the challenges posed by real-world application, as previously listed. A wind tunnel test is still a controlled environment, nonetheless all uncertainties mentioned above will appear. The peculiarity of the uncertainties might be different compared to a flight test with a full aircraft, but this does not impair a methodological evaluation significantly.

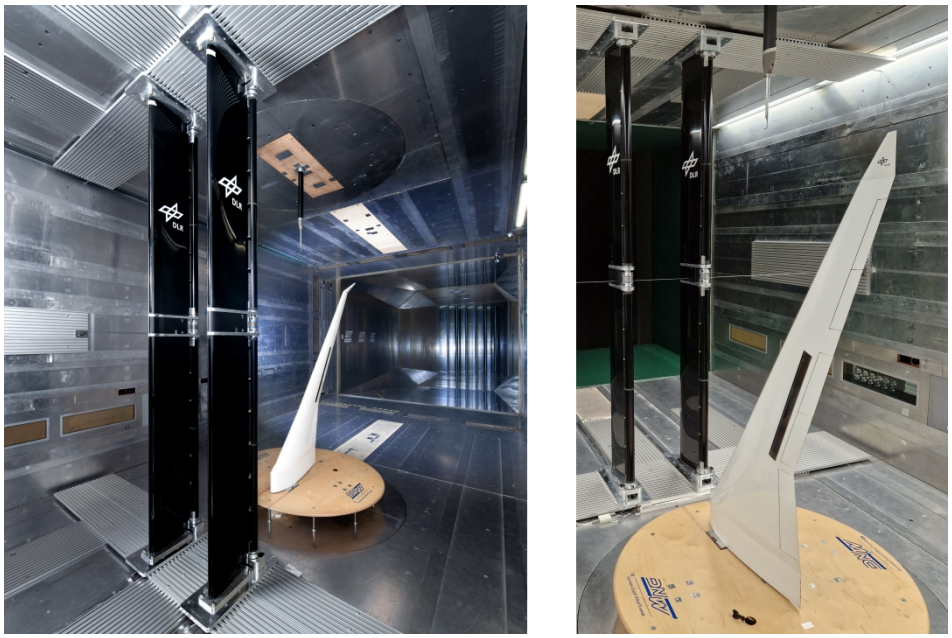

Figure 1: Experimental setup of the oLAF wind tunnel test at the DNW-NWB

The wind tunnel experiment is part of the optimally load-adaptive aircraft (oLAF) project of the German Aerospace Center (DLR), conducted in the German-Dutch Wind Tunnels (DNW) low-speed wind tunnel Braunschweig (NWB). More information on the oLAF project is given in [12]. The oLAF experimental wing is of high aspect ratio and features sweep. It is equipped with distributed accelerations sensors used for feedback control. Trailing edge flaps are deflected to achieve load alleviation. A gust generator is installed upstream of the wing, shedding vortices at a desired frequency, with the possibility for both discrete and continuous gusts. Fig-

ure 1 shows the oLAF wind tunnel setup, the five trailing edge control surfaces on the wing are visible. A detailed description of the flexible wing development is given in [13], while [14] details the concept and development of the gust generator.

The structure of this paper follows the timeline of the wind tunnel experiment. First an overview on the numerical aeroservoelastic model is given, yielding a virtual representation of the experiment. Second, this numerical model is updated with experimental data gathered in the first phase of the wind tunnel test. This includes structural dynamics, aerodynamics, as well as actuator and sensor dynamics. Third, the controller is designed using this updated model, while previous controller design iterations used the non-adapted numerical model. Last, the controller is experimentally validated. This process not only allows to test the performance of the developed GLA functionality, but also to evaluate the accuracy of the numerical model.

The challenges regarding uncertainties are addressed by employing robust control. μ-synthesis ($D$-$K$-iteration) [15] is chosen to design an unstructured controller, as it allows to balance conflicting requirements for load reduction, control activity, and robustness. Additionally, the control allocation is optimized within the synthesis. The performance target is focused on using the integral loads at the wing's root (wing-root bending and torsion moment). The model and controller design is done in MATLAB-Simulink.

## 2 AEROSERVOELASTIC MODELING

The gust load alleviation (GLA) functionality tested in the DNW-NWB is developed using model-based controller design. Therefore, a numerical aeroservoelastic model of the experimental wing is required. The modeling process is schematically shown in figure 2. A model is derived for each of the model ingredients, i.e. structural dynamics, aerodynamics, actuators, and sensors, before being integrated in the overall model. The model is available as a nonlinear simulation in the time domain for controller validation, and a linear state-space model for control synthesis. The modeling is based on the procedure outlined in [16], using the VarLoads environment [17, 18].

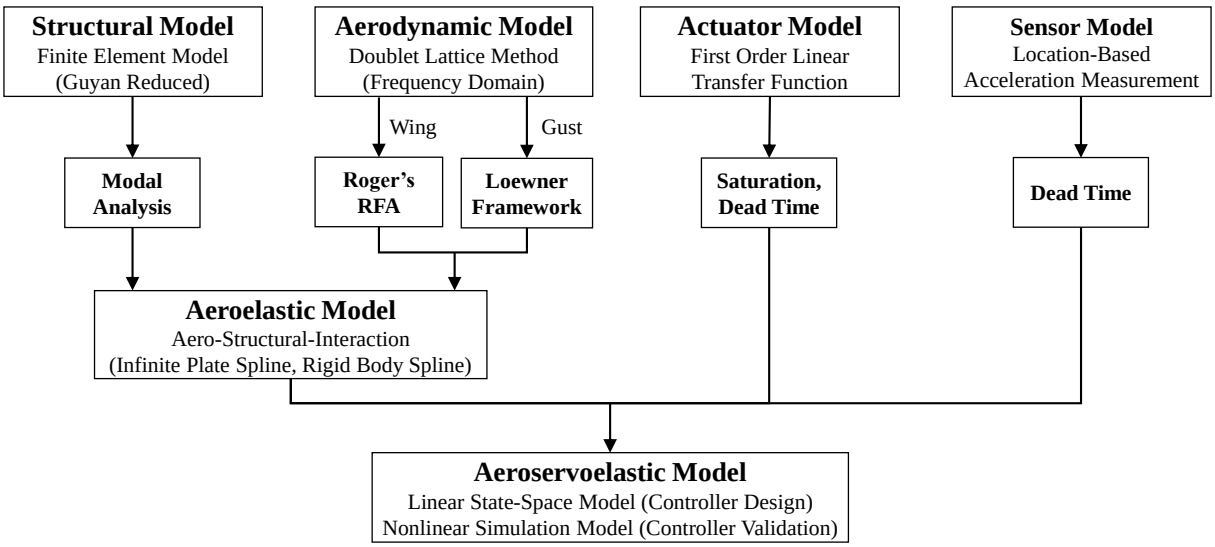


Figure 2: Schematic representation of the numeric modeling process

Developing the numerical model of the oLAF experimental wing is described in detail in [19]. Here, only an overview of the model components will be given.

### 2.1 Structural Modeling

The oLAF experimental wing is the result of a structural design and optimization process, for further details see [13]. The approach was successfully applied to previous wind tunnel projects, as detailed in [20, 21]. A numerical representation of the structural dynamics is given in form of a finite element model. This model is then condensed to a beam representation by Guyan reduction [22], from which the structural properties in form of a stiffness, damping, and mass matrix can be extracted. A modal analysis is performed to obtain eigenvalues and eigenvectors [23] and above-mentioned matrices in the modal domain. The linear elastic equation of motion (mean axis) for the flexible wing is the foundation of the aeroelastic plant [24, 25]:

$$\mathbf{M}_{ff} \cdot \ddot{\mathbf{u}}_f + \mathbf{B}_{ff} \cdot \dot{\mathbf{u}}_f + \mathbf{K}_{ff} \cdot \mathbf{u}_f = \mathbf{\Phi}_{gf}^T \cdot \mathbf{P}_g^{ext}. \tag{1}$$

Modal displacement $\mathbf{u}_f$, velocity $\dot{\mathbf{u}}_f$, and acceleration $\ddot{\mathbf{u}}_f$ depend on the modal matrix of mass $\mathbf{M}_{ff}$, damping $\mathbf{B}_{ff}$, and stiffness $\mathbf{K}_{ff}$, as well as the external forces and moments $\mathbf{P}_g^{ext}$ applied through the eigenvector matrix $\mathbf{\Phi}_{gf}$. External forces and moments are aerodynamic and gravity-induced in the wind tunnel experiment. The subscripts in the notation are taken from [26].

### 2.2 Aerodynamic Modeling

The wind tunnel experiment is conducted at sea-level atmospheric conditions with low Mach numbers (between 0.1 and 0.15), the reference speed being 30 to 50 m/s. An aerodynamic modeling based on potential flow theory is therefore assumed to be sufficiently accurate. The doublet lattice method (DLM) [27, 28] is applied on a discretized wing surface to obtain the unsteady aerodynamic forces and moments in the frequency domain [16]:

$$\mathbf{P}_g^{aero}(k) = q_\infty \cdot \mathbf{T}_{kg}^T \cdot \mathbf{S}_{kj} \cdot \underbrace{\mathbf{Q}_{jj}(k) \cdot \mathbf{w}_j}_{\mathbf{\Delta c}_{p,j}}, \qquad k = \frac{\omega \cdot c_{ref}}{2 \cdot U_\infty}. \tag{2}$$

The DLM outputs a aerodynamic-influence-cofficient (AIC) matrix $\mathbf{Q}_{jj}$ which allows to calculate the pressure difference $\mathbf{\Delta c}_{p,j}$ for each aerodynamic panel, given the downwash $\mathbf{w}_j$ on the respective panel. These AIC matrices depend on the reduced frequency $k$ [25]. Converting pressure differences to forces and moments is performed by multiplication with $\mathbf{S}_{kj}$ and the dynamic pressure $q_\infty$. The mapping between aerodynamic and structural model is taken care of by the coupling matrix $\mathbf{T}_{kg}$. The coupling applied here is described in further detail in [19]. Figure 3(a) shows the discretization of the wing and the five control surfaces into panels for application of the DLM, as well as the nodes of the Guyan reduced structural model.

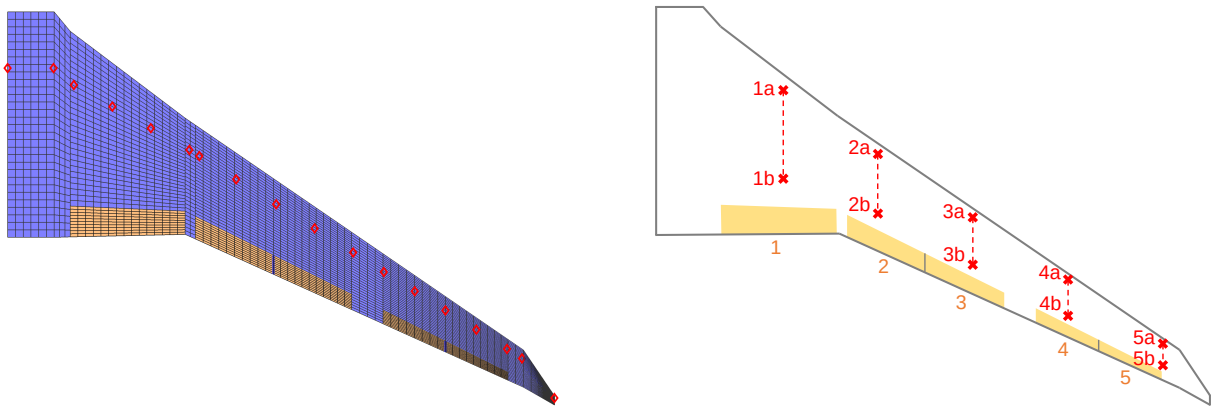


(a) Aerodynamic discretization and structural nodes (b) Location and ID of control surfaces and sensors

Figure 3: Aeroservoelastic model of the oLAF wind tunnel model

The downwash $\mathbf{w}_j$ in equation 2 is produced by the wing's motion described by the modal amplitude $\mathbf{u}_f$ and its derivatives, a control surface deflection $\mathbf{u}_x$ and its derivatives, or a gust input $w^G$. These inputs are specified as time domain signals, while equation 2 is obtained in the frequency domain. To transfer to the time domain, a rational function approximation (RFA) called Roger's method [29, 30] is applied for the wing's aerodynamics, while the gust aerodynamics are treated by the Loewner Framework [31, 32]. For a more in-depth description of the application of RFA and Loewner framework to the oLAF numerical model the reader is once again referred to [19].

In the wind tunnel experiment the gust profiles interacting with the flexible wing will be created by the gust generator depicted in figure 1. For the numerical model the gusts are more closely related to the certification, like the EASA CS-25 [33], in which a 1-$cos$ gust is defined:

$$w^G(t) = \begin{cases} \alpha^G \cdot \left(1 - \cos\left(\frac{2\pi \cdot U_\infty \cdot t}{2 \cdot H}\right)\right) & t_s \leq t \leq t_e, \\ 0 & \text{otherwise}, \end{cases} \tag{3}$$

with $U_\infty$ being the freestream velocity, $H$ the gust gradient (half gust length), $\alpha^G$ the gust angle in radians, $t_s$ the start time, $t_e$ the end time of the gust encounter. The gust angle can be selected to match the ones achievable in the experiment, while the gust gradient $H$ is varied to test for all types of gusts that potentially interact with the wing. Besides this discrete 1-$cos$ gust, also a periodic gust with a continuous sine-like excitation can be generated in the experiment, so it is also added to the numerical model.

### 2.3 Actuator Modeling

To obtain an aero*servo*elastic model, the aeroelastic model must be augmented by actuators and sensors. The design of the controller depends quite significantly on the capabilities of the actuation system, which therefore needs to be modeled accurately. The electromechanical actuators used in the oLAF experiment can be modeled by a first order linear transfer function, with added non-linearities, as proposed in [34]. A second order linear transfer function might be even more common [35], but as experience gained in a previous DLR project [10, 34] showed a first order transfer function to be sufficient, it is chosen here. An overview on the possible non-linearities occurring in an actuator is given in [35]. Here, the non-linearities taken into account are limited to saturation in deflection, rate, and acceleration, as well as dead time. The non-linearities cannot be represented in the linear state-space model used for controller design, however the dead time is approximated by a Padé element and the saturations are incorporated indirectly in the controller design weighting functions (see section 4). Figure 4 shows a schematic representation of the used actuator model.

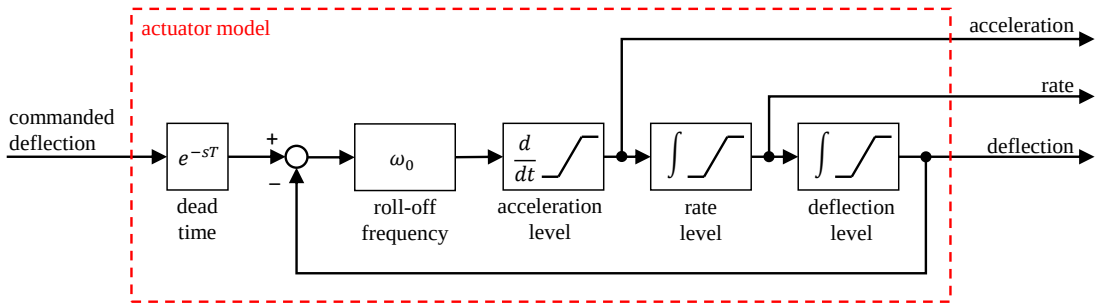


Figure 4: Schematic representation of the actuator model

The values to be chosen in the actuator model are based on the ones identified in [7] and [34] for the time being, before the actuator is identified and the model updated in preparation for the

wind tunnel test, see section 3. The roll-off frequency of the first order transfer function is set at 90 rad/s or 14.3 Hz, the deflection limit to 10°, rate limit to 1130°/s and acceleration limit to 79500°/s². The dead time is set to 4.3 ms. The same actuator type is used for each control surface on the oLAF experimental wing. Figure 3(b) shows the layout of the five actuated trailing edge flaps and the ten distributed acceleration sensors on the wing.

### 2.4 Sensor Modeling

The orientation and designation of the ten acceleration sensors used on the oLAF wing is shown in figure 3(b). The sensors are placed pairwise at five spanwise locations, always one near the leading edge and one near the trailing edge. By this layout it is possible to capture both bending and torsion with unidirectional sensors.

Within the numerical model, no dynamics of the sensors are included, as these are considered to be significantly fast and therefore negligible. The sensors outputs are modeled by determining the acceleration at the sensor location, which is done by a mapping from the condensed structural grid using rigid body splines [36]. The sensors are all oriented in the z-direction (upwards). A time delay of 1 ms is added to the sensor output. In the linear model this delay is again approximated by a Padé element. Noise can be added to the sensor output in the numerical model, to test the performance of the controller when receiving disturbed signals.

Adding actuators and sensors completes the aeroservoelastic modeling process. This model is used for controller design and validation. The next section describes how the model is updated in preparation for the experiment.

## 3 EXPERIMENTAL IDENTIFICATION AND MODEL UPDATE

To refine the controller design in preparation for the wind tunnel experiment, the numerical model is validated and updated by experimental data. Identification and model updating will occur separately for the components of the flexible wing, as displayed in figure 2, i.e. structural dynamics, actuators, and sensors. The aerodynamics cannot be identified separately, which is why these are identified last in terms of an aeroservoelastic characterization, including all the other components. This aeroservoelastic characterization is purely to check the model, not to update it, as done for the other components. The updated numerical model is used for a last iteration of controller design, which is detailed in section 4.

### 3.1 Structural Dynamics

Once the experimental wing is placed within the wind tunnel, the modal parameters of the system can be identified in order to update the structural model. Outside the wind tunnel the parameters will be very similar if the wing is clamped at its root, but the flexibility of the wind tunnel balance alters the parameters slightly. Hence, the test is carried out as soon as the wing is installed for the test.

The focus of the structural identification is on the first flexible mode - first out-of-plane wing bending - as it is the primary target of the GLA function. The second flexible mode is an out-of-plane wing bending as well, but with a significantly lower modal contribution. Higher modes were observed in frequency domain plots obtained during the experiment, but these modes only play a minor role in the dynamic behavior of the wing. The first four flexible modes of the wing as within the finite element model are presented in figure 5.

To identify the structural dynamics and to be able to correlate the measurements with the simulation, the wing needs to be excited in a controlled manner. Therefore, a unit force is applied

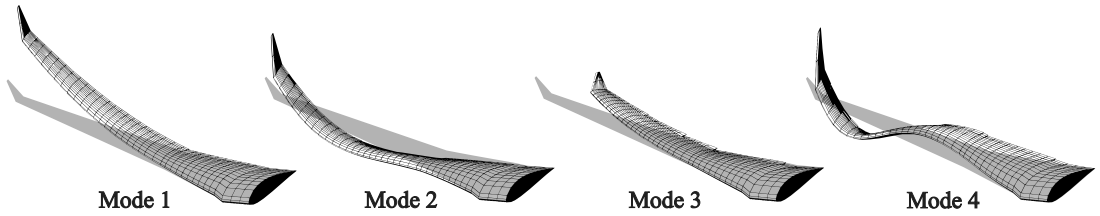

Figure 5: First four flexible eigenmodes extracted from the finite element model

near the wingtip to achieve a predefined deflection at the tip. Then, the unit force is removed instantaneously so the wing may oscillate freely, with only negligible external forces applied. The time response can then be compared to the simulation, in which the aerodynamic contribution is removed and the initial conditions are chosen to replicate the predefined deflection.

First, the measured time response of the wing is used to determine the eigenfrequencies. Applying a fast fourier transform (FFT) reveals the eigenfrequencies of the flexible wing, which is shown in figure 6, using the measurements of the wind tunnel balance corresponding to the wing-root bending moment (WRBM). Multiple time responses are used and converted to a frequency response. All of them exhibit a similar pattern, the only difference is the energy contained in the respective response. The eigenfrequency of the first flexible mode is determined to be 8.5 Hz, while the second one is at 36.5 Hz. The third eigenfrequency is at 90 Hz in the finite element model, but is not clearly identified in the FFT plot. This is because the third mode is an in-plane bending of the wing. This type of motion is not excited when applying a static unit force to the wing tip and releasing it.

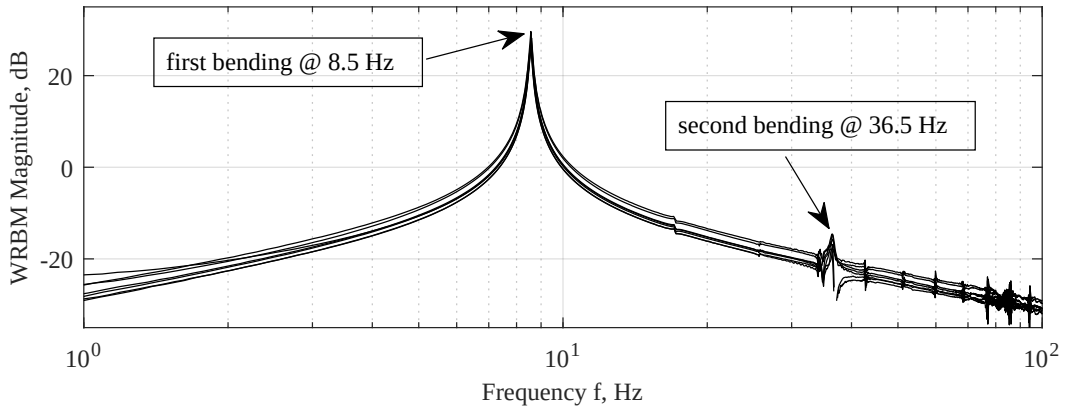

Figure 6: WRBM frequency response when releasing the wing from a predefined deflection

The eigenfrequency information is used to adapt the finite element model to match the identified properties. Before the update, first and second bending frequency were at 9.0 and 31.8 Hz, respectively. The difference to the new frequencies of 8.5 and 36.5 Hz is not too large. From the updated finite element model the updated modal stiffness matrix $\mathbf{K}_{ff}$ can be derived, featuring the square of the eigenfrequencies along its diagonal. The modal mass matrix $\mathbf{M}_{ff}$ is unity, due to orthogonality conditions [23,25]. It remains to update the modal damping matrix $\mathbf{B}_{ff}$. In the numerical model, this matrix is chosen stiffness- and mass-proportional, since structural damping is very difficult to model [25]. The damping matrix is adapted by analyzing the decay of the oscillation when releasing the wing from the static deflection. This is done in the time domain, and the first entry of the damping matrix is scaled to achieve a good match between simulation and experiment. In doing so, only the first eigenmotion is corrected in its damping. Figure 7 shows the comparison between simulation and experimental measurements when releasing the

wing from the static deflection, for the measurements of acceleration sensor 5a (wingtip, near leading edge, see figure 3(b)). Figure 7(a) is the comparison prior to the update of the modal damping matrix, figure 7(b) the one after the update. In the former, the simulation exhibits a damping that is too large, since the free oscillation decays faster than in the experiment. In the latter, simulation and measurement results match closely. This concludes the update of the structural dynamics part of the oLAF wing.

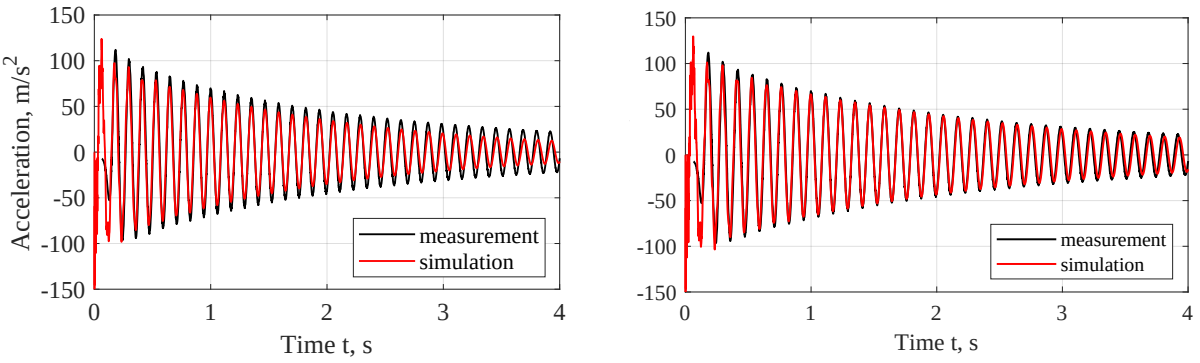


(a) Before the damping matrix update

(b) After the damping matrix update

Figure 7: Sensor 5a response when releasing the wing out of a predefined deflection with a unit force at the wingtip

### 3.2 Actuators

Aim of the actuator identification is to determine the properties used in the actuator model introduced in section 2, i.e. the linear transfer function, dead time and limits. The dead time of the actuation system is of great importance for controller design, because it directly affects stability of the controller and hence its maximum achievable performance [37]. The transfer function and limits determine how well the controller will be able to respond to a gust excitation. The identification is carried out using the wing wind tunnel model, with control surfaces attached to the actuators. Due to the different size of the control surfaces (see figure 3(b), inertial effects will differ depending on the control surface considered. However, these differences are neglected here, in favor of one actuator model to be applied to all five trailing edge control surfaces. The estimated error is small since the weight of the control surfaces is relatively low.

To determine the transfer function and dead time of the actuation system, the wing is clamped such that no motion of the wing itself can occur. A sinusoidal control surface deflection of a certain amplitude is commanded for a range of frequencies (usually called frequency sweep or sine sweep), and the actual deflection measured by a laser triangulation system pointed to the respective control surface. Relating commanded and measured response in the frequency domain by applying a FFT yields the transfer behavior in magnitude and phase. This identification procedure is adapted from [34]. The results are shown in figure 8, left for magnitude and right for phase. Three different amplitudes of deflection are tested, 1°, 3°, and 5°. Since the target of the identification is to update the controller design numerical model, the focus is on the lower frequency regime up to 12 Hz. Above 20 Hz the actuator properties deviate (not shown here), this is related to saturation in rate, acceleration, and power supply [34].

The transfer function of the actuator model will be chosen to best approximate the magnitude over frequency. The figure shows that the actuator behavior is quite similar for different amplitudes, with the 1° deflection being a little off. The magnitude response starts from 0 dB at 0 Hz, indicating ideal command to actual deflection behavior, and then drops when frequency is

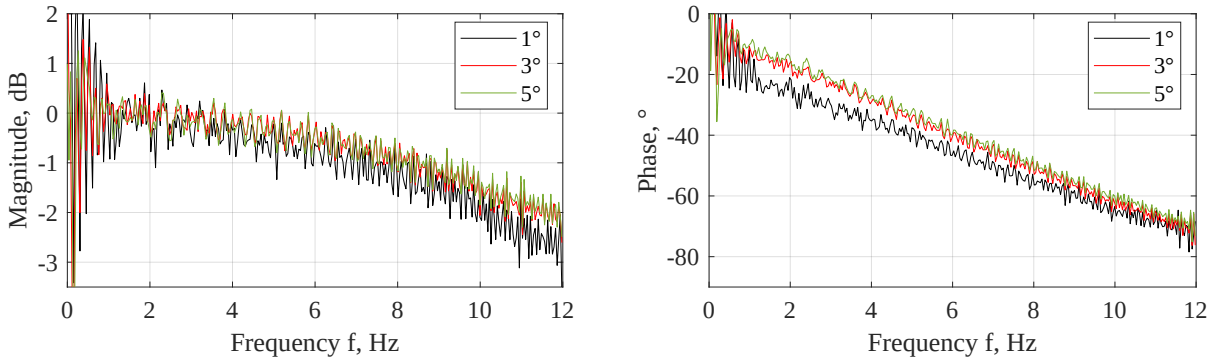


Figure 8: Frequency response of the FFT performed on the commanded to measured actuator deflection

increased. To facilitate the fitting of a first order transfer function, the FFT curves are replaced by a polynomial fit, to which the transfer function is adapted by varying the roll-off frequency $\omega_0$. Figure 9 displays the result, with a first order actuator with $\omega_0 = 14.5$ Hz found to best match the measurements. The magnitude plot of the first order model is in-between the 1° measurement fit, and the 3° and 5° measurement fit, which are almost overlapping. It can be assumed that the 1° measurements are less accurate than the ones for higher amplitudes, based on the bandwidth of the FFT shown in figure 8. Hence, the first order model is not fitted to the worst case portrayed by the 1° results, but to the 3° and 5° measurements, making sure the magnitude of these measurement is not exceeded at any frequency.

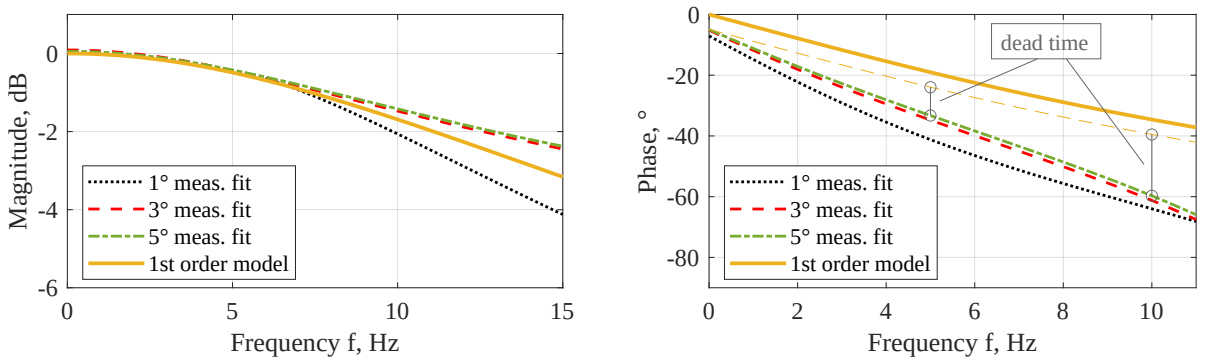


Figure 9: First order transfer function and dead time approximation for the actuator model

Turning towards the phase plot on the right in figure 9, again polynomial fits approximate the phase response for the different amplitude measurements. The first order model chosen based on magnitude is also plotted. Now, the phase plot offers to estimate dead time. There is aleady a phase offset of the measurements for a frequency of 0 Hz. This is probably attributed to freeplay or backlash [34, 35]. To separate this phenomena from dead time, the first order model is offset equally at 0 Hz, displayed by the dashed yellow line in above's figure. Dead time leads to a linear increase in phase loss over frequency, as seen by inspecting the following equation taken from [37]:

$$T_t(f) = -\frac{\angle\, G(s)}{2\pi f} \qquad \rightarrow \qquad T_t(f) = -\frac{\varphi_{model}(f) - \varphi_{meas}(f)}{2\pi f}. \tag{4}$$

Evaluating the difference in phase between the first order model (with offset to compensate for backlash) and the 5° measurement leads to a dead time of 5.2 ms at 5 Hz, and 5.6 ms at 10 Hz. For the 3° measurement it is 5.9 and 6.0 ms at 5 Hz and 10 Hz, respectively. Ideally, the dead

time would be identical, independent of the frequency at which it is evaluated. Differences might be introduced by limits and higher order dynamics in the actuator. For the actuator numerical model, it is chosen to use 6 ms of dead time.

The limit in deflection of the actuator is set by the geometric properties of the control surfaces. On the oLAF experimental wing the surfaces may deflect up to 14° in either direction. The rate and acceleration limit leads to a drop in magnitude delivered by the actuator at higher frequencies. However, as the controller will not command deflections higher than approx. 12 Hz in frequency, these limits are not crucial for controller design. Thus, these are simply taken from [34], as similar actuators were used in this experiment. The identification of the roll-off frequency and the dead time shown in above's figures was done for the middle control surface number three, and the model matches well with all other control surfaces. Table 1 summarizes the values identified above and used for the actuator model.

Table 1: Actuator properties used in first order model

| Parameter | Symbol | Value | Source |
|---|---|---|---|
| roll-off frequency | $\omega_{0,act}$ | 14.5 Hz | identified |
| dead time | $T_{d,act}$ | 6.0 ms | identified |
| deflection limit | $\delta_{max}$ | $\pm 14°$ | geometric |
| rate limit | $\dot{\delta}_{max}$ | $\pm 1130°/s$ | from [34] |
| acceleration limit | $\ddot{\delta}_{max}$ | $\pm 79500°/s^2$ | from [34] |

### 3.3 Sensors

As the acceleration sensor signals are an input for the controller, the correctness of these signals is important for the working of the GLA function. Two properties of the sensors are analyzed: signal noise and amplitude depending on sensor position. For the noise identification the acceleration measured by the sensors is recorded while the wing is not excited. This signal is shown in figure 10(a). The black line indicates the noise when the actuators are powered (with a 0° deflection command given to the actuators), the red line indicates the noise when the actuators are switched off. It can be observed that the standard deviation in noise increases from 0.17 m/s² to 0.75 m/s² when the actuators are switched on. Peaks in noise reach up to almost 3 m/s².

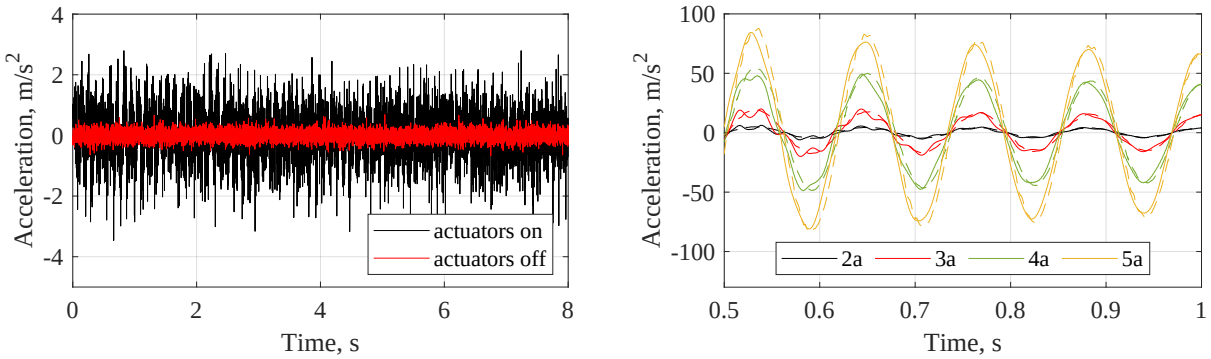


(a) Noise level with and without actuation, sensor 5a (b) Sensor signals comparison, exp. (—), sim. (- - -)

Figure 10: Sensor measurements to identify noise, signal ratios, and match with the numerical model

The frequency content of the noise is quite broad, but the main contribution occurs above 15 Hz. Additionally, a low frequency bias is observed, in a frequency regime below 2 Hz. For controller design this means that a washout and roll-off at approximately the frequencies mentioned before should be implement - either in the form of a filter or directly by the shape of the controller

transfer function. This ensures that the controller reacts only to nominal signals, and not to noise or bias.

Figure 10(b) compares the signal ratio of the sensors placed at different spanwise locations. The location of the sensors is shown in figure 3(b). The presented signals are taken during the same test as performed for the structural identification: the wing is statically deflected by a unit force applied near the wing tip, and then released from this position. The static deflection is 3.5 cm measured at the tip. The simulation replicates the experiment.

It was observed that some of the sensors delivered signals not matching the simulation, being incorrectly scaled for where the respective sensor is placed. The outermost sensors 5a and 5b matched in simulation and experiment, and hence are taken as the reference. The ratio between the outermost sensors and the more inboard sensors is taken from the simulation, and then applied to the experimental sensor signals. Thereby the signals are corrected in their magnitude to match with the simulation. Figure 10(b) shows the result of this correction process. Another information can be drawn from this figure: the ratio of sensor signals. It is obvious that the outermost sensors exhibit the highest amplitude during the oscillation. Thus, these sensors are most suitable to be used by the controller, featuring the best signal-to-noise ratio.

### 3.4 Aeroservoelastic Characterization - Combined System with Aerodynamics

Having updated the structural, actuator, and sensor model, the remaining uncertainty stems from aerodynamics. As mentioned above, the aerodynamics cannot be identified individually, instead, the entire aeroservoelastic system is characterized. The identified system is compared with the simulation, but no model update is performed. Here, only the results at a wind tunnel velocity of 30 m/s is presented, similar results were obtained at 40 and 50 m/s.

First, the steady aerodynamics are identified. Figure 11 (left) shows the WRBM over angle of attack (AoA), from experimental data as well as simulation. The markers stem from the evaluation at a distinct AoA, while the line is linear based on the slope between 0 and 2° AoA. It is chosen to present the WRBM rather than the lift force as the former is the primary quantity addressed by the load alleviation controller. At 0° AoA, already approx. 50 Nm of WRBM are present, due to the camber of the wing. Zero lift is achieved at approx. -3°. The experimentally identified WRBM slope in the depicted region is almost linear, as seen by the markers only mildly deviating off the linear slope line. The simulation is able to recreate the experimentally identified WRBM slope quite well. At 0° AoA there is a a difference of about 1 Nm, and the lift gradient is a bit steeper. This leads to a slight over-prediction of lift in the simulation, more noticeable towards higher angle of attacks.

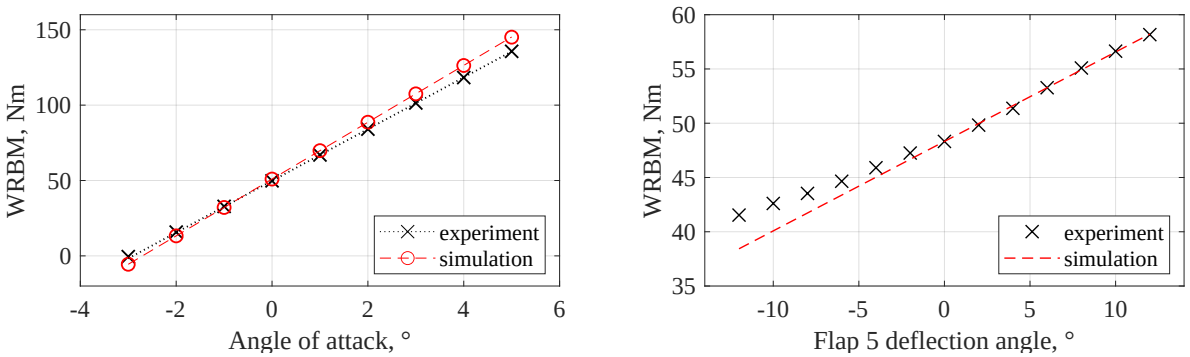


Figure 11: Angle of attack (left) and flap 5 deflection (right) effect on WRBM, experiment and simulation

The right plot in figure 11 shows the effect of a static deflection of control surface 5 is shown, and experiment and simulation are compared. The flap is deflected from -12 to +12°. The simulation exhibits a linear WRBM slope, whereas for the experiment the gradient seems to be lower for an upward deflection compared to the one for a downward deflection. However, it should be noted that the depicted flap angle is just the commanded value, and not the actual angle, since there is no measurement available for this angle. Additionally, the zero flap offset between experiment and simulation (due the difference at 0° AoA) is corrected for in this figure. The similarity between experiment and simulation is considered sufficient.

Following the steady identification, the dynamic behavior of the flap is evaluated. As for the actuator identification, a dynamic flap deflection command with increasing frequency (frequency or sine sweep) is used to determine the WRBM induced by the flap oscillating at a certain frequency. This yields the flap command to bending moment transfer function. The sine sweep is conducted from 0 to 12 Hz, as this frequency regime is most important for the GLA controller. The sine sweep command is given to the actuators, and the WRBM is measured. This time signal is transferred to the frequency domain by means of a FFT. The procedure is repeated in the simulation environment. The result of the dynamic identification for a 6° frequency sweep of flap 5 is depicted in figure 12.

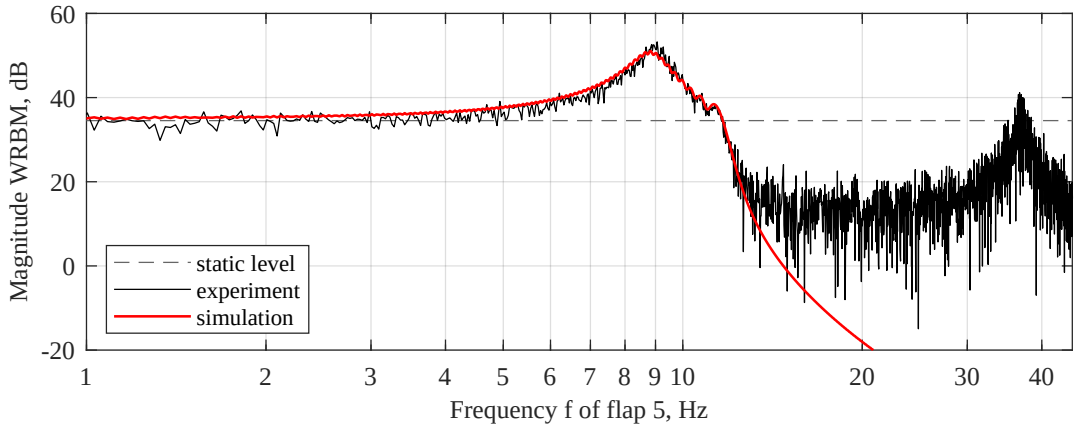


Figure 12: Frequency-dependent WRBM due to a 6° deflection of flap 5, experiment and simulation

In the figure above, the frequency response resulting from the FFT is corrected to match the static flap deflection level for low frequencies (shown by the dashed line). The bending moment frequency response starts at the static level, and increases towards 9 Hz, which is the frequency of the first flexible eigenmode of the coupled aeroservoelastic system at 30 m/s. Comparison with figure 6 reveals that by adding aerodynamics, the eigenfrequency is shifted from 8.5 to 9 Hz. After 9 Hz the magnitude drops again. Simulation and experiment match almost perfectly. Note that the difference between simulation and experiment above 12 Hz stems from the end of the frequency sweep at this frequency, so the data above 12 Hz is not representative.

Besides the bending moment, also the torsion moment and the acceleration signals are of importance for gust load alleviation. Therefore, figure 13 shows the evaluation of the wing-root torsion moment (WRTM) (left) and sensor 5a (right) for the dynamic identification, also for 6° of amplitude of flap 5. As for the bending moment, experimental data and simulation show a good match up to the frequency of 12 Hz until which the frequency sweep was performed. For the sensor a mismatch is seen in the lower frequency regime, where the simulation magnitude drops below the one of the experiment. For low frequency movements, the acceleration is very low. In the experiment, perturbations in the airflow excite the wing even for low frequencies,

which is not the case in the simulation, explaining the lower magnitude. For all sensors the match around the first flexible eigenfrequency is sufficiently accurate for controller design.

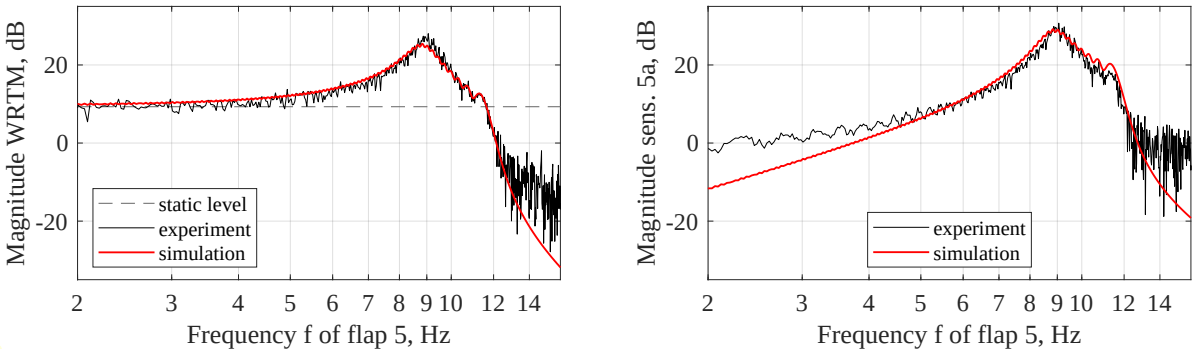


Figure 13: WRTM (left) and acceleration (right) due to a 6° deflection of flap 5, experiment and simulation

For controller design it is also beneficial to investigate the contribution of the available control surfaces. Figure 14(a) shows the comparison of the flaps for a static deflection, while figure 14(b) depicts the dynamic case. In the static case, the innermost flap 1 has the greatest effect on WRBM. The influence decreases for more outboard located control surfaces. Three effects play a role here: first, the location of the flap with respect to the wing root, second, the flap size, and third, the lift distribution across the span. The inboard flaps are larger in size, thus generate more lift, and also the lift is higher on the inboard wing compared to the outboard wing. The lever arm however increases with increasing spanwise location of the flap. In the static case the first two effects seem to dominate. In the dynamic case however, flap 5 exhibits the highest effect on WRBM around the first eigenfrequency, and the influence decreases towards the control surfaces located more inboard. Hence, in order to reduce the WRBM in the frequency regime of the first eigenfrequency, the outermost control surfaces are most effective, and hence will be used for the controller designed in section 4.

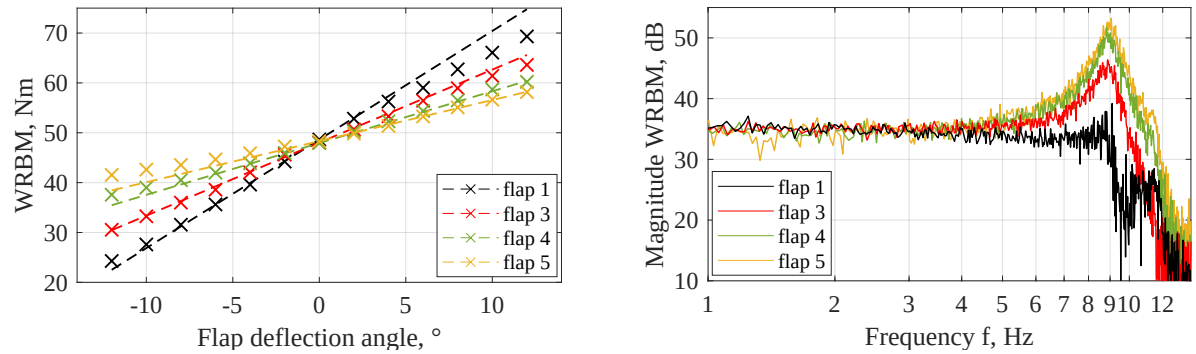


(a) Static deflection, exp. (x) and sim. (- - -)

(b) Dynamic deflection of 6°, experimental

Figure 14: Influence of the different control surfaces on WRBM, static and dynamic

### 3.5 Aeroservoelastic Characterization - Gust Interaction

The last step is to quantify the effect of gusts on the aeroservoelastic system. The gust generator shown in figure 1 consists of two symmetric profiles to align the airflow, with two rotating slotted cylinders placed behind them. Depending on the rotation frequency of the cylinders, vortices are shed and transported downstream, interacting with the flexible wing. Gusts can be generated both continuous and discrete. For the latter case the cylinders of the gust generator are rotated just once, by 180° - 720°, depending on the desired number of oscillations in the discrete event. The generated gusts are not purely sinusoidal, but contain a range of frequen-

cies, primarily exciting frequencies that are integer multiplies of the double rotation frequency. Hence, the frequency that is excited the most is twice the rotation frequency. This is shown in figure 15 for a continuous gust generator rotation at 4.5 Hz, leading to a primary gust frequency of 9 Hz. The gust angle is measured by the 5-hole probe installed above the wind tunnel model, also visible in figure 1. The time signal is shown on the left, the result of a FFT on the right. The frequency domain reveals the integer multiplies of 9 Hz being excited as well, but with a lower magnitude. Further details on the gust generator can be found in [14].

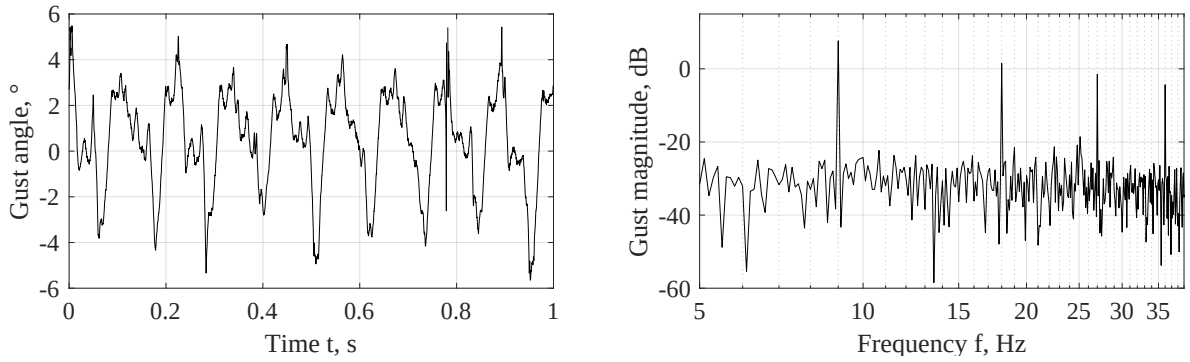


Figure 15: Gust angle at the 5-hole probe for a gust generator frequency of 4.5 Hz

For comparison with the simulation model, continuous gusts are used to construct the transfer function from gust input to forces and moments or acceleration signals. Figure 16 shows the transfer function from gust angle to WRBM. The transfer function is obtained by taking the root mean square (RMS) value of the time signal at the respective frequency (twice the gust generator rotation frequency). The experimental data is directly measured by the wind tunnel balance. The simulation data is generated by feeding the gust angle measured at the five hole probe into the model. The ideal simulation data marked by a red dashed line does not use any experimental measurements, but a gust angle of 1.8°, which was the determined mean gust angle generated in the experiment. Since the generated gust angle varies (as seen in figure 15), an uncertainty region is added to the plot, for a variation about the nominal gust angle of $\pm 0.5°$.

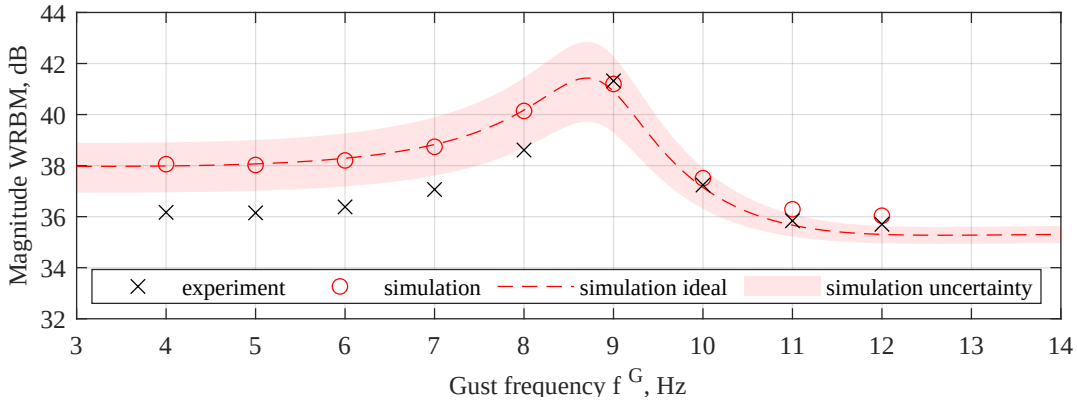


Figure 16: Gust induced WRBM, gust angle $\approx 2°$, experiment and simulation

The plot shows a good agreement between experimental and simulation data for the higher frequencies, particularly at the first eigenfrequency of 9 Hz. For lower frequencies simulation and experiment differ from one another. The simulation over-predicts the loads generated by the gust. It is not clear what causes this difference, the reason still must be investigated. The plot furthermore reveals that the ideal simulation fed by pure sinusoidal gusts at the mean gust amplitude closely matches the simulation fed with the gust angle measurements.

## 4 ROBUST GUST LOAD CONTROL DESIGN

The previous sections were devoted to the development, update and validation of the numerical model, which is used for model-based controller design. As shown in the sections above, the updated numerical model resembles the experiment in most cases with high accuracy. In contrast to the well defined wind tunnel experiment, in a free flying aircraft the aeroservoelastic system exhibits a larger degree of uncertainty, especially in aerodynamics and the external disturbance. Before the first flight of a new aircraft type, when no real world flight test data is available, a quantification of the uncertainty is difficult.

Robust control, especially $\mu$-synthesis ($D$-$K$-iteration), is a promising linear control technique to cope with these uncertainties. The idea in $\mu$-synthesis is to obtain an optimal controller with the highest performance possible, while taking defined uncertainties into account directly within the controller design process [15, 38]. Therefore, a certain level of robustness is guaranteed by this method, in opposition to other control methods that only check robustness after the synthesis with a potential need for re-tuning. The oLAF wind tunnel test allows to experimentally validate this technique for a GLA application. Another benefit of $\mu$-synthesis is that an optimal controller is obtained in which the connections of inputs and outputs is determined by the optimization algorithm. This is advantageous in aeroservoelastic control, since the measurement and control allocation is less obvious than in other control applications.

### 4.1 Control targets and generalized plant

For $\mu$-synthesis, the control problem is defined in the form of a so-called generalized plant [15]. This allows to define an optimization problem based on weighted inputs and outputs of the plant, which is augmented by uncertainties. Thus, instead of directly selecting controller gains, the control targets are reflected in weighting functions for performance, control activity, and robustness, and the optimization algorithm [38] finds the according gains. As a starting point for the generalized plant a block diagram of the wind tunnel experiment is depicted in figure 17.

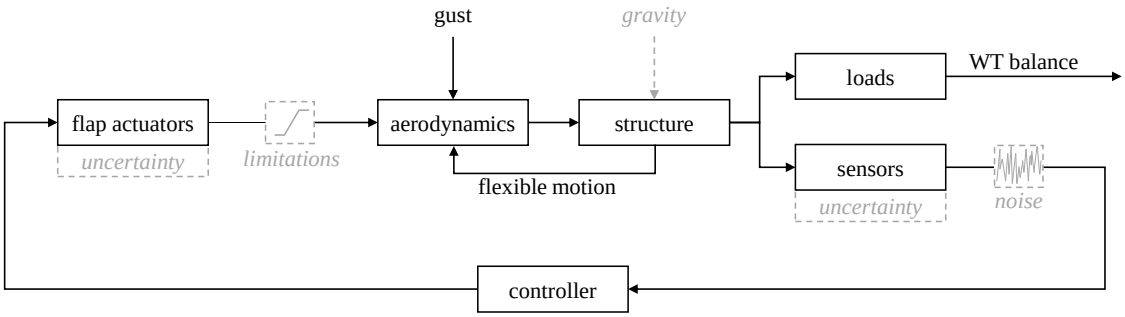


Figure 17: Block diagram of the wind tunnel experiment (gray: adaptations in controller design model)

This block diagram combines all contributions of the numerical model described in section 2 and 3. For controller design some adaptations are performed, indicated in gray (and with dashed blocks) in above's figure. The controller design model is a linear state-space model, which is why the nonlinear limitations in flap deflection, actuator rate and acceleration are not included. Neither are gravity and the acceleration sensor noise. The model is order-reduced, to reduce computational effort in the synthesis process and obtain a controller state-space model with as few states as possible. The numerical model is augmented by uncertainties, placed within the actuators and sensors. This is done to achieve robustness, and will be explained below.

Abstracting the block diagram of figure 18 to obtain the generalized plant requires to define the control targets. For gust load alleviation, these are the following:

1. reduction of the loads at the wing root: wing-root bending moment (WRBM) and wing-root torsion moment (WRTM), with more weight on the former,
2. minimization of control activity and limitation in bandwidth of the controller,
3. stability of the closed loop system,
4. robustness against uncertainties (from simplifications in the controller design model, from disturbances, from changing operating conditions, ...)
5. applicability to a range of gust gradients as well as other atmospheric disturbances.

Based on these targets and the block diagram in figure 17, the generalized plant $\mathbf{P}$ can be created, it is shown in figure 18. All blocks of figure 17 are included within the aeroservoelastic plant $\mathbf{G}$, with the exception of the controller $\mathbf{K}$ and the uncertainties of actuators and sensors. Exogenous inputs $\mathbf{w}$ and outputs $\mathbf{z}$ are defined to achieve the control targets, as explained below. The controller is closing the loop, using the sensor measurements as a feedback vector $\mathbf{v}$, outputting control commands $\mathbf{u}$. The reference signal $\mathbf{r}$ is zero in the case of GLA, as the wing should ideally remain stationary, with no acceleration present. Selection matrices $\mathbf{H}_i$ select the outputs of the plant, either acceleration signals or loads. Weighting functions are denoted $\mathbf{w}_i$, while uncertainties are denoted $\mathbf{\Delta}_i$.

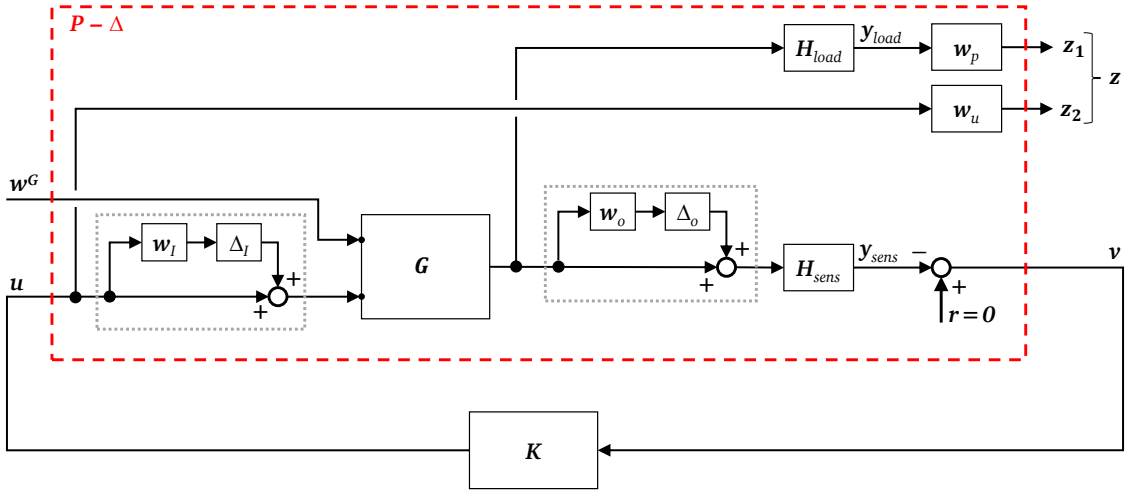


Figure 18: Generalized plant with exogenous inputs, exogenous outputs, and uncertainties

To fulfill the control targets, the following choices are made when creating the generalized plant:

1. define the wing-root loads as exogenous output $\mathbf{z}_1$, yielding a performance channel, weighted by the performance weight $\mathbf{w}_p$,
2. define the actuator commands as exogenous output $\mathbf{z}_2$, yielding a control activity channel, weighted by the control activity weight $\mathbf{w}_u$,

3./4. place multiplicative structured uncertainties [15] at the actuators and sensors, yielding a robustness channel, weighted by $\mathbf{w}_I$ and $\mathbf{w}_o$,

5. define the gust signal $w^G$ as the exogenous input, covering the frequency range of interest.

It is important for robustness to include uncertainties both at the plant input (actuators) and the plant output (sensors). Otherwise the $\mu$-synthesis might only guarantee robustness at either of the two locations within the loop, which is undesirable. This design procedure can also be motivated physically, since uncertainties might arise both in sensor measurements and flap positions. The uncertainties are implemented as multiplicative structured uncertainties (details in [15], and in [19] for the problem at hand). The uncertainty matrices $\mathbf{\Delta}_I$, $\mathbf{\Delta}_o$ only feature diagonal terms, as there is no cross-coupling between individual actuators and sensors [39].

Using the developed generalized plant, the task of finding a GLA controller is translated into the task of selecting appropriate weights for the performance, control activity and robustness channel (weighting functions $\mathbf{w}_p$, $\mathbf{w}_u$, $\mathbf{w}_I$, and $\mathbf{w}_o$).

### 4.2 Controller synthesis and outcome

The uncertainty weights can be selected based on physical insight [39]. For the actuators, the uncertainty is chosen low in the lower frequency regime, increasing to a maximum of 10% of the commanded deflection when exceeding half the roll-off frequency. For sensors, a similar shape of the uncertainty is chosen, but with an upper maximum of 5% of the measured acceleration.

Emphasizing the peak in wing-root loads occurring near the first eigenfrequency is the aim of the performance weight. The GLA controller shall primarily dampen this mode, as this brings down the gust loads most efficiently. In the lower frequency regime the loads shall not exceed the ones of the open loop, but a reduction is not necessary. Hence, the performance weight is constant up to approx. 15 Hz. A roll-off is implemented at this frequency, as the loads occurring at higher frequencies are not driving, and because the actuators are limited in their capability above their roll-off frequency. Figure 19(a) shows how the performance weight shapes the closed loop system. The curves shown represent the maximum singular value of the generalized plant, from input $w^G$ to performance output $z_1$, the performance channel. It can be seen that the peak in max. singular value is significantly reduced in the closed loop system, while open and closed loop lie on top of each other for lower frequencies.

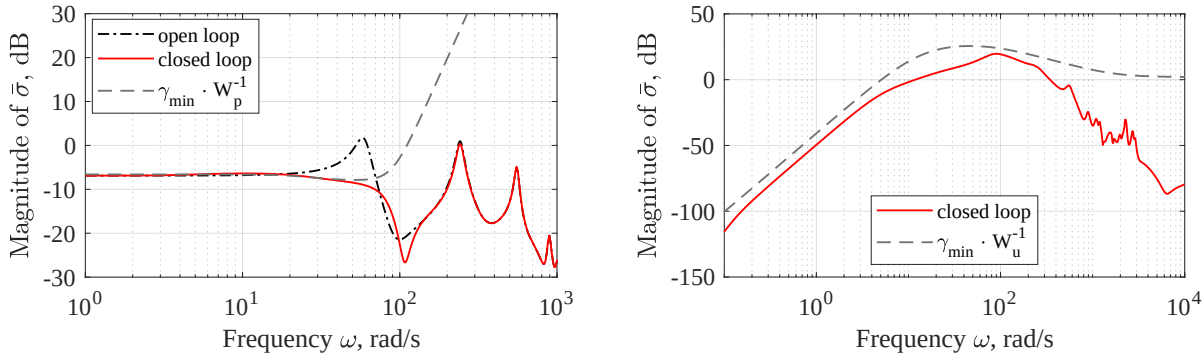


(a) Performance channel, $\mathbf{w}$ to $\mathbf{z}_1$

(b) Control activity channel,$\mathbf{w}$ to $\mathbf{z}_2$

Figure 19: Performance and control activity weight shaping the closed loop response

For the control activity weight a shape is selected that allows the controller to be active in the central frequency regime (around the first eigenfrequency), while featuring a washout towards low and a roll-off towards high frequencies. The washout is important to avoid the bias introduced by the sensors, while the roll-off avoids the sensor noise, as outlined in section 3.3. Furthermore, this shape of control function is selected to avoid static control surface deflection as well as an actuator command that is too fast. Figure 19(b) details how this weight shapes the closed loop control activity channel.

The $\mu$-synthesis ($D$-$K$-iteration) algorithm will use the defined generalized plant to find an optimal controller in form of a state-space model. During the synthesis, an iterative process is executed, alternating between a $H_\infty$-synthesis ($K$-step) [40] and a $\mu$-analysis ($D$-step) [41]. The $K$-step finds an optimal controller based on the generalized plant's transfer function, while the $D$-step adapts this transfer function to incorporate sufficient robustness under the defined uncertainties. Therefore, the algorithm takes care of performance, control activity, and robust-

ness requirements simultaneously. More information of the $\mu$-synthesis applied to the oLAF experiment is given in [19].

The $\mu$-synthesis robust controller presented here will use the outermost acceleration sensors 5a, 5b, and the outer two control surfaces 4, 5 to achieve load alleviation (see figure 3(b)). The outer two control surfaces best resemble ailerons on a current transport aircraft. Other controller variants using different sets of sensors and control surfaces were tested, but will not be discussed here. One advantage of robust control is that once the top level requirements are cast into the weighting functions of the generalized plant, the closed loop system will exhibit a behavior relatively independent of the sensors and actuators being available (within limitations).

Figure 20(a) shows the comparison of open and closed loop, in terms of the maximum singular value from exogenous input to all exogenous outputs. As discussed for the performance channel depicted in figure 19(a), the controller is able to significantly reduce the peak in bending moment. The closed loop is exceeding the open loop for the frequency range form 70 to 100 rad/s, but this is of no concern as the loads are comparatively low in this regime.

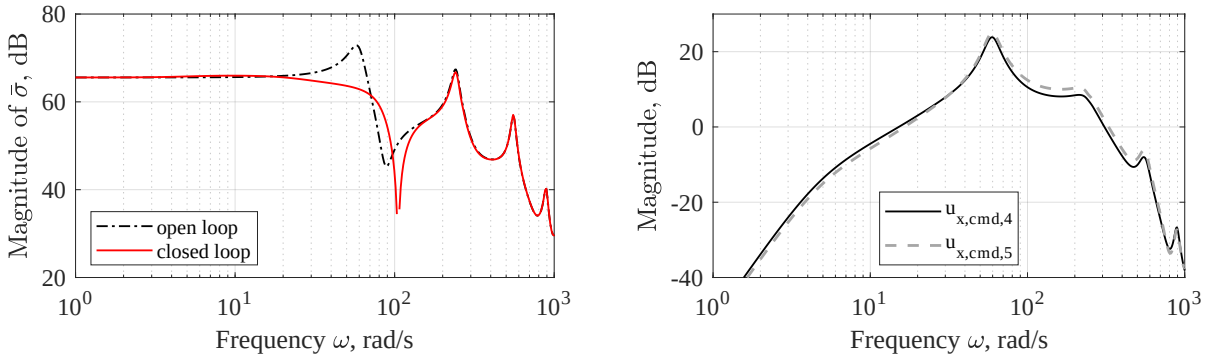


(a) Open and closed loop max. singular value

(b) Controller transfer function, $w^G$ to $\mathbf{u}_x$

Figure 20: Result of $\mu$-synthesis: open and closed loop max. singular value and controller transfer function

Figure 20(b) shows the frequency response of the controller transfer function, more specifically from a gust input $w^G$ to the control commands of the outer two flaps. The washout towards low and roll-off towards high frequencies as demanded by the control activity weight (figure 19(b)) is visible. Most control activity is achieved at the first bending frequency of 9 Hz.

It remains to evaluate the robustness of the controller. This is done by disk-based stability margins, as introduced in [42]. These margins are calculated at the input and the output of the plant $\mathbf{G}$, and summarized in table 2. Both multiloop margins - assuming simultaneous disturbances in all channels - and loop-at-a-time margins - only one channel is disturbed - are evaluated. The time delay of actuator, sensors and controller hardware (8 ms in total) is present in the evaluation. The margins are sufficient to call the developed controller robust. The match of input and output margins indicates a balanced design achieving maximum performance.

Table 2: Disk-based stability margins of the open loop transfer function

| Type | Cut point | Gain margin | Phase margin | Frequency | Worst loop |
|---|---|---|---|---|---|
| multiloop | input | $0.46 \mid 2.17$ | $-40.5° \mid 40.5°$ | 14.9 Hz | - |
| multiloop | output | $0.46 \mid 2.17$ | $-40.6° \mid 40.6°$ | 14.9 Hz | - |
| loop-at-a-time | input | $0.29 \mid 3.45$ | $-57.7° \mid 57.7°$ | 16.0 Hz | $u_{x,cmd,5}$ |
| loop-at-a-time | output | $0.28 \mid 3.62$ | $-58.4° \mid 58.4°$ | 16.0 Hz | $\ddot{u}_{m,5b}$ |

## 5 EXPERIMENTAL RESULTS OF ROBUST GUST LOAD CONTROL

The developed controller is tested in the wind tunnel experiment. As described in section 3.5, the gust generator mounted upstream of the wing injects continuous or discrete gusts at a certain frequency. The controller is executed on a real-time system running at a sample frequency of 1000 Hz. The acceleration signals are supplied to the controller, which outputs control commands to be executed by the actuators at a rate of 560 Hz. A data acquisition system records the measurements, including wind tunnel balance forces and moments, acceleration signals, control commands, and other commands. All experimental results are generated at a wind tunnel speed of 30 m/s.

The wind tunnel balance captures the loads using the following definition of axes: the x-axis points in the direction of the flow, the y-axis along the span of the wing, and the z-axis completes the right hand coordinate system (aerodynamic coordinate system). This yields a positive lift force if the lift acts upwards, a positive wing-root bending moment if the wing is deflected upwards, and a positive torsion moment if the wing is deflected nose-up. It shall be noted that the wing-root torsion moment shown in the following is taken at the wind tunnel balance, i.e. the coordinate system is aligned with the airflow and not the loads reference axis. Thus, the torsion moment more resembles a pitching moment.

### 5.1 Continuous Gusts

First, the controller performance under continuous gusts shall be evaluated. The gust generator is continuously turning, injecting a harmonic, sine-like gust into the airflow. To demonstrate the effect of the active GLA controller, a measurement is performed for a time of 40 s, with the controller initially turned off. The controller is switched on after approx. 12.5 s, gradually increasing its gain, until a gain of one is reached. The controller is kept activated until 27.5 s, at which it is turned off again. Figure 21 shows the WRBM signal resulting from this measurement, corrected to exhibit zero mean.

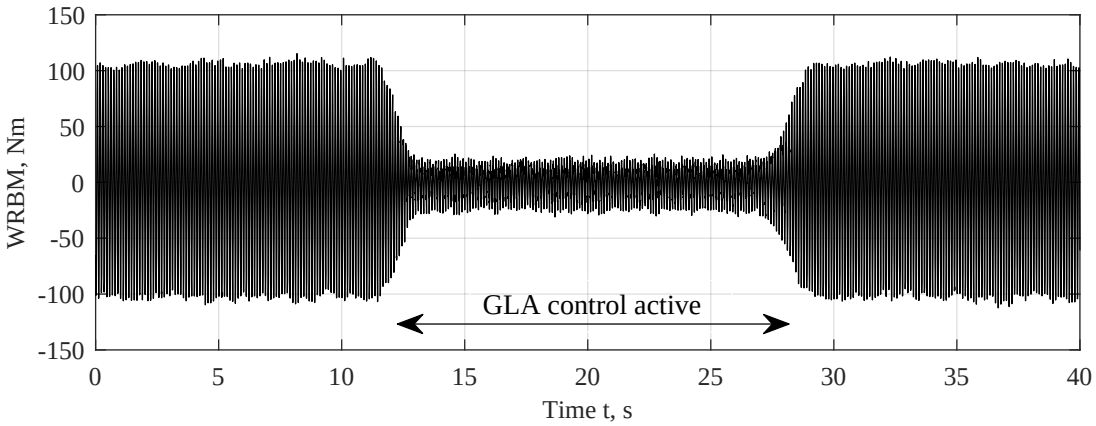


Figure 21: Wing-root bending moment during a continuous gust excitation with 9 Hz

Activating the gust load controller results in a significant decrease in wing-root bending moment. The RMS value is decreased from 71.5 to 13.6 Nm, resulting in a relative reduction of 81%. If the static WRBM of approx. 50 Nm is taken as a reference (see figure 11(a)) the reduction from 121.5 to 63.6 Nm results in a relative reduction of 47%. It shall be noted that this reduction is the best case, achieved when the gust excites the first eigenfrequency of 9 Hz. For other frequencies the reduction is less, but still significant, as discussed further below.

Figure 22 (left) shows the reduction in WRBM more detailed, focusing on a time section of one second. The RMS reduction from 71.5 to 13.6 Nm is also observable here. Besides the bending moment, also the torsion moment at the wing root is of importance for the structural loads. The comparison for torsion without and with active controller is presented on the right of figure 22. The scaling of the y-axis is the same as on the right, to be able to compare the order of magnitude of the two moments. It is visible that the bending moment is almost twice as large as the torsion moment. The controller not only reduces the bending moment, but also the torsion moment. The reduction from a RMS of 43.6 to 8.2 Nm when the controller is switched on yields a 81% decrease, as for the bending moment. With a static level of -30 Nm, the relative reduction becomes 48%. The bending-torsion coupling present on a backward swept wing is assisting in bringing the torsion moment down by control action. A negative (upward) control deflection reduces the bending moment, such that the nose-down induced torsion moment due to the bending-torsion coupling is also reduced. Additionally, the upward deflection of the control surfaces leads to more lift shifted forward, also counteracting the nose-down torsion moment.

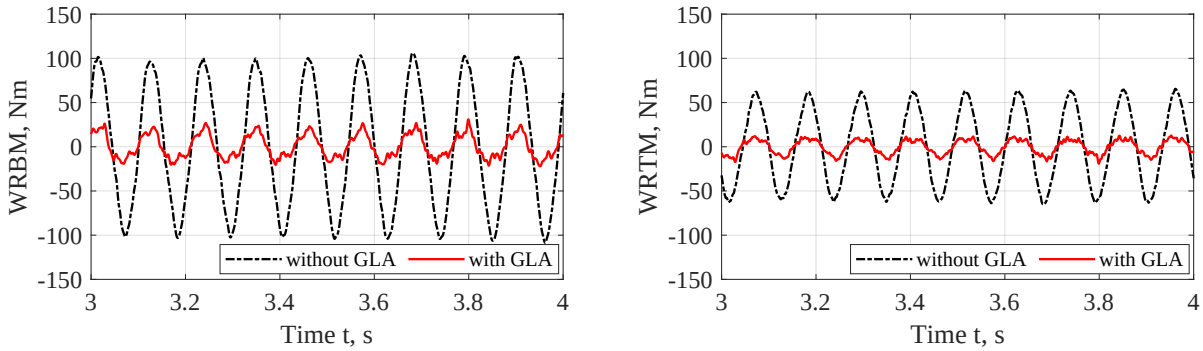


Figure 22: Wing-root bending (left) and torsion moment (right), with and without GLA, gust frequency 9 Hz

The reduction in loads is generated by the deflection of the control surfaces. Once deflected upwards (negatively), the lift is decreased by adding camber, which in turn loads to lower wing root forces and moment. Figure 23 shows the commanded control surface deflection of the outer two flaps. The controller makes equal use of both flaps. This is plausible, as figure 14(b) in section 3.4 shows equivalent dynamic contribution of these two flaps to the WRBM. Both control surfafces are used only slightly more than 10°, which yields a safe margin to the maximum deflection angle of 14°. The portrayed case depicts the highest control surface deflections, as it is taken for a 9 Hz gust excitation. When comparing figure 23 to figure 22, a slight phase shift between the peaks in moments and the peak in control commands is observed. This is because the controller uses the accelerations as an input, which are zero at the peak moments, and largest at the moment's zero crossing.

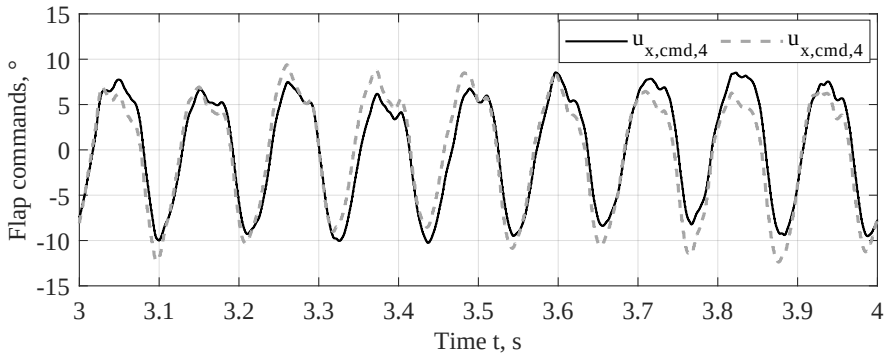


Figure 23: Control surface commands during a continuous gust excitation with 9 Hz

Gust loads shall not only be decreased for one gust gradient (i.e. one gust frequency), but for the entire frequency regime of interest. For this experiment, this range is approx. from 6 to 12 Hz. Figure 24 depicts the experimental and simulation results for the case with and without GLA, for multiple gust frequencies. The plot is obtained in the same fashion as outlined in section 3.5. For experimental data, the measured time signal is transfer to the frequency domain by calculating the RMS value. The simulation results are obtained by feeding the gust angle measured by the 5-hole probe into the simulation and also determining the RMS of the output time signal. The dashed line representing the simulation results is a fit through the discrete points of gust frequencies, in order to facilitate the readability of the plot.

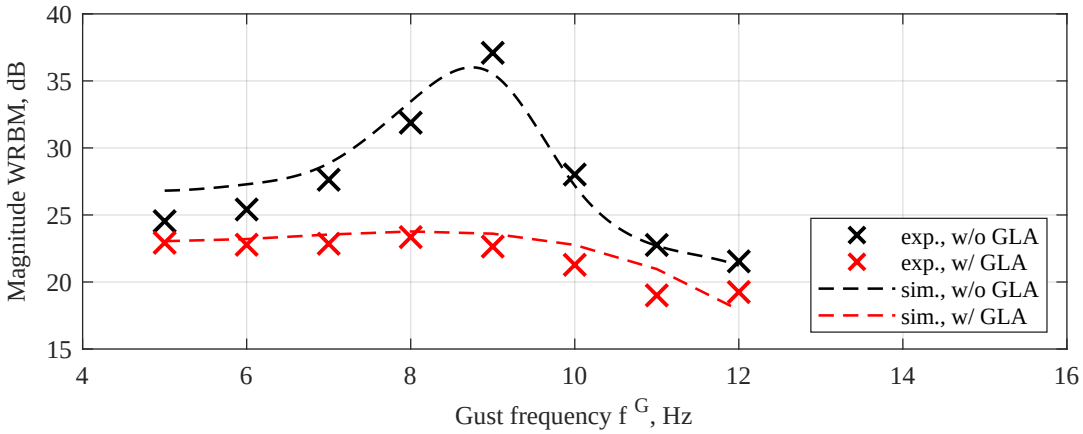


Figure 24: Magnitude of WRBM with and without GLA at multiple gust frequencies, exp. and sim.

The experimental data confirms that the controller successfully reduces gust loads not only at 9 Hz, but for all frequencies under investigation. The reduction is undoubtedly largest around the first eigenmode, but in all cases the open loop signal is larger than the closed loop signal. Towards lower frequencies, the controller reduces the loads only slightly, this is desired as not to interfere with primary flight control. In a free flying aircraft, the rigid body dynamics would absorb a large portion of the loads from low frequency gusts, i.e. the wing-root loads would not be that high. Since the wind tunnel model is clamped, this rigid body motion load relief is not portrayed in the experiment.

Experimental and simulation data match very well. As already discussed in section 3.5, deviations occur for the open loop case below a gust frequency of 9 Hz. For the closed loop case the match seems to be even better.

### 5.2 Discrete Gusts

Continuous gusts producing a harmonic, sine-like excitation are rather academic, and typically do not occur in flight. Hence, it is important to evaluate the controller performance under discrete gusts as well. These are generated by a one-time rotation of the gust generator. Turning the gust generator by 180° yields a single gust peak, while a rotation of 720° yields four gust amplitudes. The results for the former case are shown in figure 25, for a gust excitation of 9 Hz. The wing-root bending moment is shown on the left, for open and closed loop, the corresponding control action on the right.

The results confirm the effectiveness of the controller not only for continuous, but also for discrete gusts. A 60% reduction could be achieved by reducing the bending moment from approx. 40 to 16 Nm. Note that for the discrete event the peak value of the WRBM is lower than for the continuous gust. With the reference value of 50 Nm at 0° AoA, the relative reduction

reads 27%. The reduction is achieved by a flap deflection not larger than 7°, as seen on the right plot of figure 25. The control activity after the decay of the discrete gust event is caused by the gust generator still injecting disturbances into the airflow, only this time with a more undefined frequency spectrum.

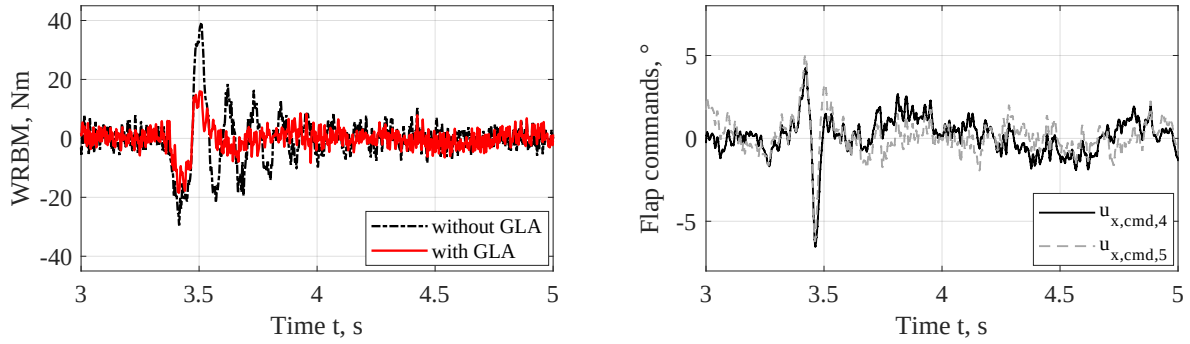


Figure 25: WRBM (left) and flap commands (right), for a discrete gust with 9 Hz, 180° rotation of gust gen.

Moving to the 720°, the results are shown in figure 26. It is noted that this case is somewhat intermediate between the 180° discrete event and the continuous gust discussed above. The controller is capable to reduce the loads by a similar percentage as for the 180° case. In the WRBM plot it is visible that the controller is particularly effective in damping the oscillations after the four gust peaks have passed, in contracts to the remaining free oscillation of the uncontrolled wing. As before, the control commands do not exceed 10°.

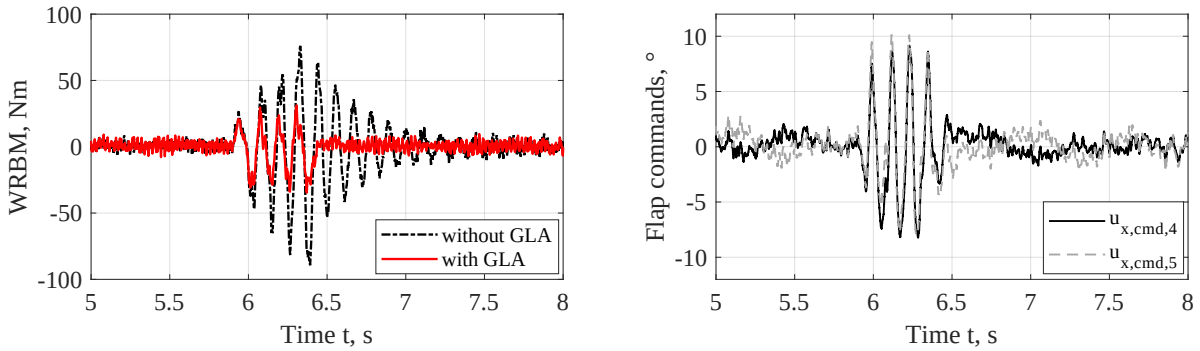


Figure 26: WRBM (left) and flap commands (right), for a discrete gust with 9 Hz, 720° rotation of gust gen.

The experimental evaluation proved the satisfactory load reduction capabilities of the controller, while adhering to the constraints in flap deflection and robustness, demonstrating the successful application of $\mu$-synthesis robust control for gust load alleviation.

## 6 SUMMARY AND OUTLOOK

This paper describes the experimental validation of a GLA controller in a wind tunnel test, using $\mu$-synthesis robust control. The test is performed in the scope of DLR's optimally load-adaptive aircraft (oLAF) project. A swept wing derived from a high-aspect ratio transport aircraft equipped with trailing edge flaps and acceleration sensors is tested within the DNW-NWB, in which a rotating slotted cylinder gust generator is installed. The paper aims to give a full overview on the activities of the active control test. Starting point is a simulation model used for model-based controller design, including structural dynamics, aerodynamics, gust disturbances, actuators, and sensors. This model is then updated using experimental data from the identification campaign in the wind tunnel. Structural dynamics, actuators and sensor prop-

erties are updated, yielding a simulation model that closely resembles the experimental data obtained in static and dynamic wind tunnel tests. The transfer functions of the controller design model from the inputs of gust and control surface deflection command to the outputs of wing root loads and acceleration functions are thereby validated. Particular attention is paid to the actuator model, in order to determine both roll-off frequency as well as dead time, since these quantities drastically affect performance and stability of the closed loop system. By the established identification procedure, it is possible to achieve an accurate actuator model, and simulation model in general. The model is then used for controller design with $\mu$-synthesis, and finally validated in the wind tunnel.

Multiple control surfaces and sensors are available for controller design. In this paper the controller uses only the outer two acceleration sensors near the wing tip and the outer two control surfaces, resembling outboard ailerons of a transport aircraft. The controller achieves good load alleviation properties, being able to reduce the wing-root bending moment up to 80% for the case of continuous gusts, and 60% for discrete gusts. These values are achievable at a gust frequency close to the first flexible eigenfrequency of the wing, at which a peak in gust induced loads is present in the uncontrolled system. This peak is successfully reduced by applying the developed controller, and load reduction is also sufficient for other gust frequencies. The $\mu$-synthesis allows to incorporate robustness requirements in the design, and with a disk-based multiloop gain margin above two and phase margin above 40°, robustness is validated.

Future publications will examine the control design method in further detail. $\mu$-synthesis is based on top level requirements, leaving the selection of input output connections within the controller as well as actuator and sensor usage to an optimization algorithm. In the experiment multiple variants of robust controllers with different sets of actuators and sensors were tested. These cases will be evaluated in the upcoming publication.

On the way to mature active load alleviation, two primary fields are identified for further research. One is the validation of GLA at transsonic speeds. In this speed regime the aerodynamics exhibit nonlinearities (for example from pressure shocks), which may effect controller design. Research is being conducted in the EU-funded Clean Aviation project UPWing, planning a transsonic wind tunnel experiment for gust load alleviation [43]. The second field of interest is the combination of secondary functions like load alleviation with the aircraft's primary flight control system. As aircraft with high-aspect ratio wings exhibit ever lower flexible eigenfrequencies, a frequency separation strategy - independently designing primary and secondary flight control - holds no longer valid. Research at DLR is investigating this.

The oLAF experiment demonstrates the practical applicability of active load alleviation, contributing to next generation control technologies to be deployed on future transport aircraft.

## 7 ACKNOWLEDGMENTS

The authors would like to thank all contributors involved in planning, preparation and execution of this wind tunnel experiment, making the active gust load alleviation test possible. Special thanks to Holger Mai and Marc Braune (test execution, measurement technology and data acquisition), Tania Kirmse (image-based measurements, to be evaluated for further publications), Julius Sieg (aeroelastic identification of the model), Wolf R. Krüger (co-project lead of oLAF), and the team of the DNW-NWB.

## 8 REFERENCES


[1] Binder, S. (2021). *Simultaneous Optimisation of Composite Wing Structures and Control Systems for Active and Passive Load Alleviation*. PhD thesis, Delft University of Technology, Delft, The Netherlands. doi:10.4233/uuid:fac93ccf-7e0b-4971-a797-d2617e378a1d.

[2] Ramsey, H. and Lewolt, J. (1979). Design maneuver loads for an airplane with an active control system. In *Proceedings of the 20th Structures, Structural Dynamics, and Materials Conference*. St. Louis, USA: AIAA, pp. 456–463. doi:10.2514/6.1979-738.

[3] Regan, C. D. and Jutte, C. V. (2012). Survey of applications of active control technology for gust alleviation and new challenges for lighter-weight aircraft. Technical Report, TM-2012-216008, NASA. https://ntrs.nasa.gov/citations/20120013450.

[4] Chin, J. (1990). Universal-type gust alleviation system for aircraft. U.S. Patent 4905934. Grumman Aerospace Corporation. https://www.freepatentsonline.com/4905934.html.

[5] Fournier, H. et. al. (2022). Robust gust load alleviation of flexible aircraft equipped with lidar. *Journal of Guidance, Control, and Dynamics*, 45(1). doi:10.2514/1.G006084.

[6] Wang, X., van Kampen, E., Chu, Q. P., et al. (2019). Flexible aircraft gust load alleviation with incremental nonlinear dynamic inversion. *Journal of Guidance, Control, and Dynamics*, 42(7). doi:10.2514/1.G003980.

[7] Pusch, M. (2020). *Blending of Inputs and Outputs for Modal Control of Aeroelastic Systems*. Ph.D. thesis, Hamburg University of Technology (TUHH), Hamburg, Germany. https://elib.dlr.de/139100/.

[8] Fezans, N., Joos, H.-D., and Deiler, C. (2019). Gust load alleviation for a long-range aircraft with and without anticipation. *CEAS Aeronautical Journal*, 10, 1033–1057. doi: 10.1007/s13272-019-00362-9.

[9] Giesseler, H.-G., Kopf, M., Varutti, P., et al. (2012). Model predictive control for gust load alleviation. *IFAC Proceedings Volumes, 4th IFAC Conference on Nonlinear Model Predictive Control*, 45(17), 27–32. doi:10.3182/20120823-5-NL-3013.00049.

[10] Pusch, M., Ossmann, D., Dillinger, J., et al. (2019). Aeroelastic modeling and control of an experimental flexible wing. In *Proceedings of the AIAA Scitech 2019 Forum*. San Diego, USA: AIAA. doi:10.2514/6.2019-0131.

[11] Poussot-Vassal, C., Demourant, F., Lepage, A., et al. (2017). Gust load alleviation: Identification, control, and wind tunnel testing of a 2-D aeroelastic airfoil. *IEEE Transactions on Control Systems Technology*, 25(5), 1736–1749. doi:10.1109/TCST.2016.2630505.

[12] Krüger, W. R., Mai, H., Kier, T., et al. (2024). Assessment of active load control approaches for transport aircraft - simulation and wind tunnel test. In *International Forum on Aeroelasticity and Structural Dynamics (IFASD 2024)*. Den Haag, The Netherlands.

[13] Dillinger, J., Mai, H., Krüger, W. R., et al. (2024). Design, manufacturing and identification of an actively controlled flexible wing for subsonic wind tunnel testing. In *International Forum on Aeroelasticity and Structural Dynamics (IFASD 2024)*. Den Haag, The Netherlands.

[14] Schmidt, T. G., Dillinger, J., Ritter, M., et al. (2024). Design and experimental characterization of a gust-generator concept with rotating-slotted cylinders in the low-speed wind tunnel DNW-NWB. In *International Forum on Aeroelasticity and Structural Dynamics (IFASD 2024)*. Den Haag, The Netherlands.

[15] Skogestad, S. and Postlethwaite, I. (2005). *Multivariable Feedback Control*. Chichester, United Kingdom: John Wiley & Sons, 2nd ed. ISBN 978-0-470-01168-3.

[16] Kier, T. and Looye, G. (2009). Unifying manoeuvre and gust loads analysis models. In *International Forum on Aeroelasticity and Structural Dynamics (IFASD 2009)*. Seattle, USA. https://elib.dlr.de/97798/.

[17] Hofstee, J., Kier, T., Cerulli, C., et al. (2003). A variable, fully flexible dynamic response tool for special investigations (VarLoads). In *International Forum on Aeroelasticity and Structural Dynamics (IFASD 2003)*. Amsterdam, Netherlands. https://elib.dlr.de/12206/.

[18] Kier, T. M. and Hofstee, J. (2004). VarLoads - eine Simulationsumgebung zur Lastenberechnung eines voll flexiblen, freifliegenden Flugzeugs. In *Deutscher Luft- und Raumfahrtkongress (DLRK 2004)*. Dresden, Germany: DGLR.

[19] Stalla, F., Kier, T. M., Looye, G., et al. (2024). Aeroservoelastic modeling and robust control for gust load alleviation of an experimental wing. In *Proceedings of the AIAA SciTech 2024 Forum*. Orlando, USA: AIAA. doi:10.2514/6.2024-1442.

[20] Dillinger, J. K. S., Meddaikar, Y. M., Lübker, J., et al. (2017). Design and optimization of an aeroservoelastic wind tunnel model. *Fluids*, 5(1), 35. doi:10.3390/fluids5010035.

[21] Dillinger, J., Meddaikar, Y. M., Lepage, A., et al. (2022). Structural optimization of an aeroelastic wind tunnel model for unsteady transonic testing. *CEAS Aeronautical Journal*, 13, 951–965. doi:10.1007/s13272-022-00612-3.

[22] Guyan, R. J. (1964). Reduction of stiffness and mass matrices. *AIAA Journal*, 3(2). doi:10.2514/3.2874.

[23] Géradin, M. and Rixen, D. J. (2015). *Mechanical Vibrations*. New Jersey, USA: Wiley, 3rd ed. ISBN 978-1-118-90020-8.

[24] Reschke, C. (2006). *Integrated Flight Loads Modelling and Analysis for Flexible Transport Aircraft*. Ph.D. thesis, University of Stuttgart, Stuttgart, Germany. doi:10.18419/opus-3733.

[25] Wright, J. R. and Cooper, J. E. (2015). *Introduction to Aircraft Aeroelasticity and Loads*. Chichester, United Kingdom: Wiley, 2nd ed. doi:10.1002/9781118700440.

[26] Rodden, W. P. and Johnson, E. H. (1994). *MSC/NASTRAN Aeroelastic Analysis User's Guide*. MSC, 2nd ed. ISBN 978-1-585-24006-7.

[27] Albano, E. and Rodden, W. P. (1969). A doublet-lattice method for calculating lift distributions on oscillating surfaces in subsonic flows. *AIAA Journal*, 7(2). doi:10.2514/3.5086.

[28] Blair, M. (1992). A compilation of the mathematics leading to the doublet lattice method. Technical Report, ADA256304, United States Air Force Wright Laboratory. https://apps.dtic.mil/sti/citations/ADA256304.

[29] Roger, K. L. (1977). Airplane math modeling methods for active control design. In *AGARD Conference Proceedings 228*. Advisory Group For Aerospace Research and Development of NATO (AGARD).

[30] Karpel, M. (1982). Design for active flutter suppression and gust alleviation using state-space aeroelastic modeling. *AIAA Journal*, 19(3). doi:10.2514/3.57379.

[31] Mayo, A. and Antoulas, A. C. (2007). A framework for the solution of the generalized realization problem. *Linear Algebra and its Applications*, 425. doi:10.1016/j.laa.2007.03.008.

[32] Antoulas, A. C., Lefteriu, S., and Ionita, A. C. (2017). A tutorial introduction to the loewner framework for model reduction. In Peter Brenner et al. (Ed.), *Model Reduction and Approximation*, chap. 8. Philadelphia, USA: Society for Industrial and Applied Mathematics (SIAM), pp. 335–376. doi:10.1137/1.9781611974829.ch8.

[33] European Union Aviation Safety Agency (2023). Certification specification and acceptable means of compliance for large aeroplanes (CS-25). Amendment 27. https://www.easa.europa.eu/en/certification-specifications/cs-25-large-aeroplanes.

[34] Tang, M., Böswald, M., Govers, Y., et al. (2021). Identification and assessment of a nonlinear dynamic actuator model for controlling an experimental flexible wing. *CEAS Aeronautical Journal*, 12. doi:10.1007/s13272-021-00504-y.

[35] Fielding, C. and Flux, P. K. (2003). Non-linearities in flight control systems. *The Aeronautical Journal*, 107. doi:10.1017/S0001924000013543.

[36] Mauermann, T. (2011). Flexible aircraft modelling for flight loads analysis of wake vortex encounters. Technical Report, DLR-FB 2010-37, German Aerospace Center (DLR). doi:10.24355/dbbs.084-201109120959-0.

[37] Lunze, J. (2020). *Regelungstechnik 1*. Springer Vieweg, 12th ed. ISBN 978-3-662-60746-6. doi:10.1007/978-3-662-60746-6.

[38] Doyle, J. C. (1985). Structured uncertainty in control system design. In *24th IEEE Conference on Decision and Control*. Fort Lauderdale, USA, pp. 260–265. doi:10.1109/CDC.1985.268842.

[39] Bennani, S., Looye, G., and Mulder, J. A. (1997). RCAM design challenge presentation document: the μ-synthesis approach. Technical report TP-088-11, GARTEUR.

[40] Doyle, J. C., Glover, K., Khargonekar, P. P., et al. (1989). State-space solutions to standard $H_2$ and $H_\infty$ control problems. *IEEE Transactions on Automatic Control*, 34(8). doi:10.1109/9.29425.

[41] Doyle, J. (1982). Analysis of feedback systems with structured uncertainties. *IEE Proceedings, Pt. D, Control Theory and Applications*, 129(6). doi:10.1049/ip-d.1982.0053.

[42] Seiler, P., Packard, A., and Gahinet, P. (2020). An introduction to disk margins [lecture notes]. *IEEE Control Systems Magazine*, 40. doi:10.1109/MCS.2020.3005277.

[43] Timmermans, H., Jurisson, A., Eberle, A., et al. (2024). A high aspect ratio wind tunnel model for transonic gust load alleviation with active control. In *International Forum on Aeroelasticity and Structural Dynamics (IFASD 2024)*. Den Haag, The Netherlands.

## COPYRIGHT STATEMENT